Fourier-Based Multi-Agent Formation Control to Track Evolving Closed Boundaries

Bin Zhang, Hui Zhi, Jose Guadalupe Romero, *Member, IEEE*, Luiza Labazanova, Anqing Duan, Xiang Li, *Senior Member, IEEE*, and David Navarro-Alarcon, *Senior Member, IEEE*

Abstract—The automatic monitoring/tracking of environmental boundaries by multi-agent systems is a fundamental problem that has many practical applications. In this paper, we address this problem with formation control techniques based on parametric curves that represent the boundary's feedback shape. For that, we approximate the curve with truncated Fourier series, whose finite coefficients are utilized to characterize the curve's shape and to automatically distribute the agents along it. These feedback Fourier coefficients are exploited to design a new type of formation controller that drives the agents to form desired curves. A detailed stability analysis is provided for the proposed control methodology, considering both fixed and switching multi-agent topologies. The reported numerical simulation and experimental studies demonstrate the performance and feasibility of our new method to track closed boundaries of different shapes.

Index Terms—Multi-agent systems, robotics, formation control, Fourier series, sensor-based control.

I. INTRODUCTION

THE control of multi-agent systems (MAS) is a challenging problem on which many researchers have made multiple fundamental contributions over the last few decades [1], [2]. Traditional control problems in MAS include consensus, formation control, task allocation, synchronization, etc. [3]. Our focus in this paper is to study the development of new formation control strategies to position multiple robotic agents along closed parametric curves whose shape may smoothly change over time. This problem differs from standard formation controls in that the explicit target location for each agent is not known in advance, and thus, needs to be automatically solved from the curve's parametric geometry.

Formation controls can be categorized (based on the agents' sensing capabilities and interaction topologies) into the following three strategies [4]: position-based, displacement-based, and distance-based controls. Position-based strategies (which are the most widely used among the three) calculate the desired formation for the MAS using absolute position vectors [4]. In this paper, we extend this basic idea and show how finite
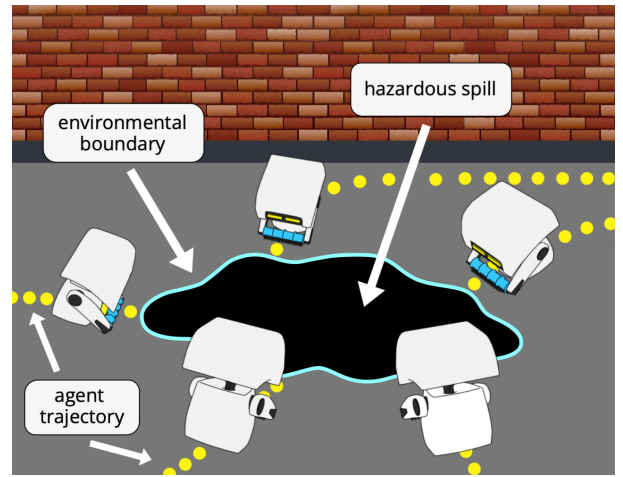
Fig. 1. Conceptual representation of a MAS approaching a closed boundary.

Fourier coefficients [5] (computed from a parametric contour defined in absolute coordinates) can be instead used to specify a desired formation, a strategy that effectively solves the lack of an explicit position target for each agent.

Formation controls are typically used to coordinate the motion of a variety of systems such as spacecraft [6], unmanned aerial vehicles (UAV) [7], [8], mobile robots [9], vessels and underwater systems [10], etc. One practically important application of formation control is the spatial monitoring of environmental boundaries, which is particularly critical e.g., to sample the spread of oil and dangerous chemicals during accidental spills [11], or to contain the boundaries of wildfires [12], see Fig. 1. As these regions may possibly be large in size, it is difficult to monitor them with a single autonomous robot; The use of MAS can significantly improve the efficiency of this task. Our goal in this paper is precisely to develop controls for these types of evolving curve-based formations.

A. Related Work

Formation control is one of the most popular control problems in MAS (see [4] for a comprehensive review). State-of-the-art methods include [13], which proposes a position-based controller for vehicles subject to second-order dynamics; [14] proposes a similar position-based strategy but for aerial vehicles. Representative examples of displacement-based controllers include [15] which presents a method to coordinate autonomous unmanned vehicles (AUVs) with optical sensors, and [16] which studies the maneuvering and robustness of

undirected control topologies. Examples of distance-based strategies are presented in [17], [18] for various conditions and applications. There are some works on formation tracking control, such as [9], [19], yet, they mostly focus on driving followers to track leaders' trajectories rather than driving agents to track evolving parametric boundaries. Formations computed with standard position-based strategies typically consist of discrete targets represented in absolute coordinates. Those computed with displacement/distance-based strategies do the control via *relative* inter-agent spatial configurations. However, these approaches may not be the most efficient way to distribute the agents along a boundary, whose most natural representation is a parametric curve. In our boundary-constrained formation problem, the agents must align along this parametric curve and automatically distribute according to the curve's arc length, an objective that clearly contrasts with that of traditional formation controls.

Various related works have addressed similar contour-based scenarios. Some early examples include [20], which propose contour-based controls for homogeneous AUVs to track profiles of plumes. However, these methods require gradient measurements, which are difficult to obtain in practice. The method in [21] adopts the idea of active contour models from the image processing to compute a motion planner that guides robots into boundaries. The algorithm in [22] uses the advection-diffusion equation to model the dynamics of plumes and to control a team of robots that monitor them. The method in [23] describes a solution to estimate time-varying boundaries with multiple robots. More examples can be found in [24], [25], where plume tracking and wildfire boundary monitoring with MAS are studied. Most previous works in the literature mainly focus on detecting/estimating the boundaries, do not exploit the properties of parametric curves in their design, have not considered the situation in which robots interact with switching topologies. Furthermore, they mostly focus on theoretical analysis, and very few conduct real-world experiments to verify the proposed methodology. The aim of this paper is to fill these gaps in the literature.

B. Our Contribution

In this paper, we propose a new control method to autonomously align a network of agents into an evolving parametric curve while keeping a desired arc length separation among them. The curve is represented with truncated Fourier series, whose "feedback coefficients" are used to establish a shape control loop. The main contributions of our work are summarized as follows:

1) A new representation of formation tasks with homogeneous MAS based on finite Fourier coefficients.
2) A new formation controller that explicitly uses Fourier coefficients to drive the agents towards the desired curve under fixed and switching topologies.
3) A rigorous stability analysis, numerical simulation and experimental study to investigate the properties and validate the performance of the proposed method.

Compared with existing works, our approach doesn't require explicit position targets for the agents. Instead, our proposed control method defines the formation in terms of a parametric curve (which can be simply obtained from an image) and drives the robots towards this target shape based on errors of Fourier coefficients (this represents a new type of servo-loop for formation control tasks).

C. Notation

Matrices and vectors are denoted as bold capital and small letters, respectively, e.g., $\mathbf{M}$ and $\mathbf{m}$. We use $[\mathbf{M}]_{ij}$ to denote the ith row jth column entry of a matrix $\mathbf{M}$, and $[\mathbf{m}]_i$ to denote the ith element of a vector. $\mathbf{I}$ denotes the identity matrix of appropriate dimension and $\mathbf{0}_{m \times n}$ is the $m \times n$ matrix of zeros. We use $\lambda_{\min}(\mathbf{M})$ to denote the minimum eigenvalue of a matrix $\mathbf{M}$.

D. Organization

The remainder of this paper is organized as follows. Section II models the parametric curves. Section III derives the proposed formation controller. Section IV presents the conducted simulation and experimental results. Section V provides final conclusions.

II. CURVE REPRESENTATION

A. The Observed Boundary

Our interest in this paper is to study formation control strategies to drive agents toward closed planar curves. Therefore, the first step is to obtain the reference boundary. In actual missions, boundaries could be predefined or obtained from top-view images of a scene. Without loss of generality, we assume that these boundaries can be characterized as a time-dependent parametric equation of the form [26]:

$$\mathbf{c}(s,t) = [c_x(s,t), c_y(s,t)]^\mathsf{T} \in \mathbb{R}^2 \tag{1}$$

for $s \in [0,1]$ as the nondimensional parameter, and t as the time variable. $c_x(s,t)$ and $c_y(s,t)$ are the 2D position coordinates of a point along this curve assumed to be measurable. Since the curve is closed, it satisfies $\mathbf{c}(0,t) = \mathbf{c}(1,t)$.

B. Curve Approximation

An intuitive way to automatically drive the agents and distribute them uniformly along the boundary of interest is to parameterize it by its arc length [27]. However, a very accurate characterization of the observed contour (1) may require a large number of frequency terms, which invariably leads to complicated (and high dimensional) geometric representations. To deal with this issue, in our method, we use an approximation of the curve, which we denote as $\tilde{\mathbf{c}}$ for a new parameter $\tilde{s} \in [0,1]$. The approximation $\tilde{\mathbf{c}}$ is obtained by fitting $\mathbf{c}$ with the following truncated Fourier series.

$$\tilde{c}_x = \sum_{h=1}^{H} [a_h \cos 2\pi h\tilde{s} + b_h \sin 2\pi h\tilde{s}] + e$$

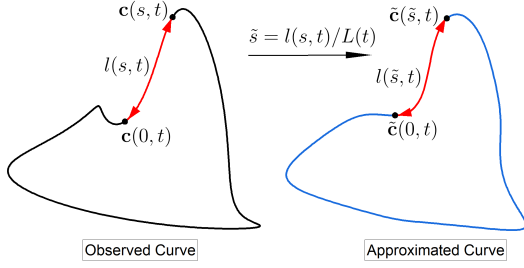$$\tilde{c}_y = \sum_{h=1}^{H} [c_h \cos 2\pi h\tilde{s} + d_h \sin 2\pi h\tilde{s}] + f \tag{2}$$

Fig. 2. The conceptual process of the curve approximation.

Fig. 3. (a) The change of coordinates; (b) Assigning arc length parameter to agents.

where H is the number of harmonics, and a_h, b_h, c_h, d_h, e, f are the Fourier coefficients. The term $\tilde{\mathbf{c}} = [\tilde{c}_x, \tilde{c}_y]^\mathsf{T}$ denotes the 2D coordinates of a point along the approximated curve.

The parameter $\tilde{s}$ is defined as the normalized arc length of the observed curve (1), and it satisfies:

$$\tilde{s} = l(s,t)/L(t) \tag{3}$$

for $L(t) > 0$ as the time-varying perimeter of the curve $\mathbf{c}$, $l(s,t)$ as the *metric* length of a curve section with the parameter range of $[0, s]$. This approximation is depicted in Fig. 2.

For convenience in further processing, we rewrite (2) as a linear regression equation of the form:

$$\tilde{\mathbf{c}} = \mathbf{G}(\tilde{s})\boldsymbol{\xi} \tag{4}$$

where $\boldsymbol{\xi} = [\boldsymbol{\rho}_1, \ldots, \boldsymbol{\rho}_H, e, f]^\mathsf{T} \in \mathbb{R}^{(4H+2)\times 1}$ denotes the vector of parameters that characterize the curve, with $\boldsymbol{\rho}_h = [a_h, b_h, c_h, d_h]^\mathsf{T}$ ($h = 1, \ldots, H$) as the Fourier coefficients, and $[e, f]$ as the offset. The regression-like matrix $\mathbf{G}(\tilde{s}) = [\mathbf{g}_1, \ldots, \mathbf{g}_H, \mathbf{I}] \in \mathbb{R}^{2 \times (4H+2)}$ contains the harmonic terms, for

$$\mathbf{g}_h = \begin{bmatrix} \cos(2\pi h\tilde{s}) & \sin(2\pi h\tilde{s}) & 0 & 0 \\ 0 & 0 & \cos(2\pi h\tilde{s}) & \sin(2\pi h\tilde{s}) \end{bmatrix} \tag{5}$$

In (4), $\boldsymbol{\xi}$ is unknown and needs to be calculated. For that, we sample discrete points along the observed curve and stack them into a point sequence $\mathbf{C} \in \mathbb{R}^{2N \times 1}$ of the form:

$$\mathbf{C} = [\mathbf{c}_1^\mathsf{T}, \ldots, \mathbf{c}_N^\mathsf{T}]^\mathsf{T} \tag{6}$$

where $N > 0$ is the total number of the sampled points.

For each point $\mathbf{c}_p$ ($p = 1 \ldots N$) in (6), we can obtain an arc length parameter $\tilde{s}_p$ by using (3), thus obtain a matrix $\mathbf{G}(\tilde{s}_p)$. We then stack these matrices into a similar sequence of the form:

$$\mathbf{G}_h = [\mathbf{G}(\tilde{s}_1)^\mathsf{T}, \ldots, \mathbf{G}(\tilde{s}_N)^\mathsf{T}]^\mathsf{T}. \tag{7}$$

We calculate the Fourier coefficients by

$$\boldsymbol{\xi} = (\mathbf{G}_h^\mathsf{T}\mathbf{G}_h)^{-1}\mathbf{G}_h^\mathsf{T}\mathbf{C}. \tag{8}$$

Note that the number of sample points along the curve must satisfy $N > 2H+1$ to guarantee the existence of $(\mathbf{G}_h^\mathsf{T}\mathbf{G}_h)^{-1}$, and thus, the boundedness of $\boldsymbol{\xi}$.
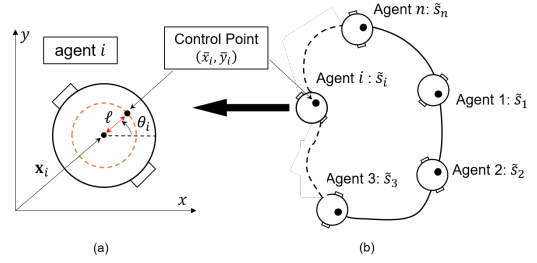
III. FOURIER-BASED FORMATION CONTROL

A. Graph Theory

The topology of the interactions among agents can be depicted by a graph, where agents are the nodes of the graph and interactions are the edges of the graph. The graph is denoted as $\mathcal{G} = (\mathcal{V}, \mathcal{E}, a_{ij})$, where a_{ij} are the weights of the interactions with the subscript ij indicating the i-th and j-th agents, $\mathcal{V} = \{1, 2, \ldots, n\}$ is the set of node indexes, n is the amount of agents, and $\mathcal{E} = \{(i,j) \in \mathcal{V} \times \mathcal{V} : a_{ij} \neq 0\}$ denotes the set of edges. Given a graph, it is called an undirected graph if $a_{ij} = a_{ji}$, otherwise, it is a directed graph [4].

For a specific agent i in the multi-agent system, we denote its neighbors by $\mathcal{N}_i = \{j \in \mathcal{V} : a_{ij} \neq 0\}$. The degree of agent i is defined as the sum of weights of its neighbors, denoted by $d_i = \sum_{j \in \mathcal{N}_i} a_{ij}$. The interconnection of agents is established by the Laplacian matrix $\mathbf{L} \in \mathbb{R}^{n \times n}$, where

$$[\mathbf{L}]_{ij} = \begin{cases} d_i, & \text{if } i = j \\ -a_{ij}, & \text{if } i \neq j \end{cases} \tag{9}$$

$a_{ij} > 0$ if $j \in \mathcal{N}_i$ and $a_{ij} = 0$ otherwise [28].

B. Controller Design

The agents considered in this work are assumed to conduct planar motions and have nonholonomic dynamics. We use $[\mathbf{x}_i^\mathsf{T}, \theta_i]^\mathsf{T}$ to describe the configuration of agent i, where $\mathbf{x}_i = [x_i, y_i]^\mathsf{T}$ and θ_i denote the center position and the orientation of agent, respectively. The dynamic model of agent i is given by [29]:

$$\begin{bmatrix} \dot{x}_i \\ \dot{y}_i \\ \dot{\theta}_i \end{bmatrix} = \begin{bmatrix} \cos\theta_i & 0 \\ \sin\theta_i & 0 \\ 0 & 1 \end{bmatrix} \mathbf{u}_i \tag{10}$$

where $\mathbf{u}_i = [v_i, \omega_i]^\mathsf{T}$ represents the control input, with v_i and ω_i as the linear and angular velocities of the agent, respectively.

To simplify our controller derivation, let us introduce the following (shifted) virtual control point [30]:

$$\begin{cases} \bar{x}_i := x + \ell\cos\theta_i \\ \bar{y}_i := y + \ell\sin\theta_i \\ \bar{\theta}_i := \theta_i \end{cases} \tag{11}$$

for an *arbitrary* scalar distance $\ell > 0$ that translates the agent's position to an arbitrary close location, see Fig. 3(a).

By using these new coordinates, we can construct the state vector $\bar{\mathbf{x}}_i = [\bar{x}_i, \bar{y}_i]^\mathsf{T}$, whose time derivative yields a modified dynamic model of the form:

$$\begin{cases} \dot{\bar{\mathbf{x}}}_i = \mathbf{R}_i(\theta_i)\mathbf{u}_i \\ \dot{\theta}_i = \omega_i \end{cases} \tag{12}$$

for a full-rank matrix defined as:

$$\mathbf{R}_i(\theta_i) = \begin{bmatrix} \cos\theta_i & -\ell\sin\theta_i \\ \sin\theta_i & \ell\cos\theta_i \end{bmatrix} \tag{13}$$

By defining a new control input $\bar{\mathbf{u}}_i = \mathbf{R}_i(\theta_i)\mathbf{u}_i$, the position dynamics in (12) can be reduced to a single integrator $\dot{\bar{\mathbf{x}}}_i = \bar{\mathbf{u}}_i$. This enables us to represent the position dynamics of the multi-agent system as follows:

$$\dot{\bar{\mathbf{x}}} = \bar{\mathbf{u}} \tag{14}$$

for an extended position vector $\bar{\mathbf{x}} = [\bar{\mathbf{x}}_1^\mathsf{T}, \ldots, \bar{\mathbf{x}}_n^\mathsf{T}]^\mathsf{T} \in \mathbb{R}^{2n\times 1}$ and an extended input $\bar{\mathbf{u}} = [\bar{\mathbf{u}}_1^\mathsf{T}, \ldots, \bar{\mathbf{u}}_n^\mathsf{T}]^\mathsf{T} \in \mathbb{R}^{2n\times 1}$. The control input of the original dynamics can be simply computed as $\mathbf{u} = \mathbf{R}^{-1}\bar{\mathbf{u}}$, with a matrix $\mathbf{R} = \mathrm{diag}(\mathbf{R}_1, \ldots, \mathbf{R}_n)$.

To ensure that the agents have an equal arc length separation between neighboring agents along the curve, we uniformly discretize the arc length parameter $\tilde{s}$ according to the number of agents, that is, the discretization step is $\mathrm{d}\tilde{s} = 1/n$. Then, we obtain a sequence of arc length parameters corresponding to the distribution for each agent:

$$\bar{\mathbf{s}} = [\tilde{s}_1, \ldots, \tilde{s}_i, \ldots, \tilde{s}_n]^\mathsf{T} \tag{15}$$

where the ith length is calculated as $\tilde{s}_i = (i-1)\mathrm{d}\tilde{s}$. The assigning of arc length parameters is shown in Fig. 3(b). Substituting the sequence $\bar{\mathbf{s}}$ into $\mathbf{G}(\tilde{s})$, we similarly obtain the sequence of harmonic matrices corresponding to each agent as follows:

$$\bar{\mathbf{G}} = [\mathbf{G}(\tilde{s}_1)^\mathsf{T}, \ldots, \mathbf{G}(\tilde{s}_i)^\mathsf{T}, \ldots, \mathbf{G}(\tilde{s}_n)^\mathsf{T}]^\mathsf{T}. \tag{16}$$

Problem Statement: By using the extended position $\bar{\mathbf{x}}$ and matrix (16), we can define the agents' position error:

$$\bar{\mathbf{x}}_e = \bar{\mathbf{x}} - \bar{\mathbf{G}}\boldsymbol{\xi} \tag{17}$$

and the curve's coefficient error:

$$\boldsymbol{\xi}_e = \bar{\mathbf{G}}^+\bar{\mathbf{x}} - \boldsymbol{\xi} \tag{18}$$

where $\bar{\mathbf{G}}^+$ denotes the pseudoinverse of $\bar{\mathbf{G}}$. The control objective is to design a Fourier-based feedback control input $\bar{\mathbf{u}}$ for the dynamics (14) that ensures the tracking of an evolving boundary $\tilde{\mathbf{c}}(t)$, i.e., the convergence of $\bar{\mathbf{x}}_e$ and $\boldsymbol{\xi}_e$ as $t \to \infty$.

Remark 1: Note that the term $\bar{\mathbf{G}}\boldsymbol{\xi}$ can be interpreted as the target positions of the agents along a curve. In our proposed method, we codify the target shape in terms of frequency terms (i.e., the Fourier coefficients) $\boldsymbol{\xi}$, which can be obtained e.g., from an image contour.

Remark 2: The rationale of ensuring the convergence of $\bar{\mathbf{x}}_i$ instead of $\mathbf{x}_i$. As is shown in Fig.3, we can always ensure that the virtual control point is within the body of the agent by appropriately selecting the distance ℓ. In that case, the convergence of the virtual control point naturally means the agent's convergence to the tracked boundary. However, it

should be noted that ℓ can not be zero, otherwise, the existence of the inverse matrix $\mathbf{R}^{-1}$ does not hold.

Since the interaction topology of the agents is represented by a graph $\mathcal{G}$ with the Laplacian $\mathbf{L}$, by combining (14) with (16) we can design the following Fourier-based formation controller to drive the agents towards the reference curve:

$$\bar{\mathbf{u}}_i = -k_1 \sum_{j\in\mathcal{N}_i} a_{ij}\left[\mathbf{G}(\tilde{s}_i) - \mathbf{G}(\tilde{s}_j)\right]\boldsymbol{\xi}_e - k_2[\bar{\mathbf{x}}_i - \mathbf{G}(\tilde{s}_i)\boldsymbol{\xi}] \tag{19}$$

where $k_1, k_2 > 0$ are feedback control gains. The first term on the right-hand side of (19) drives the agents to form the target shape of the curve. The remaining terms compensate for the relative distances between the agents and the reference curve.

C. Stability Analysis

We can rewrite the controller (19) and express it as the control input $\bar{\mathbf{u}}$ for the whole multi-agent system:

$$\bar{\mathbf{u}} = -k_1\bar{\mathbf{L}}\bar{\mathbf{G}}\boldsymbol{\xi}_e - k_2(\bar{\mathbf{x}} + \bar{\mathbf{G}}\boldsymbol{\xi}) \tag{20}$$

where $\bar{\mathbf{L}} = \mathbf{L} \otimes \mathbf{I}$ is the extended Laplacian matrix, and $\otimes$ denotes the Kronecker product. The stability analysis of the proposed controller is based on the following assumptions:

Assumption 1: The graph $\mathcal{G}$ that captures the interaction topology of the multi-agent system is strongly connected and undirected [2].

Assumption 2: The rank of the matrix $\bar{\mathbf{G}} \in \mathbb{R}^{2n\times(4H+2)}$ must always satisfy $\mathrm{rank}(\bar{\mathbf{G}}) = \min\{2n, 4H+2\}$.

Assumption 3: As the observed curve evolves, the approximated curve is updated with a constant sampling period using the processes described in Sec. II-B. The observed curve evolves at a slow speed such that we can regard the coefficients $\boldsymbol{\xi}$ as constant during the sampling period.

With Assumption 1, we ensure that the Laplacian of the graph $\mathcal{G}$ is symmetric positive semi-definite, i.e. the eigenvalues of $\mathbf{L}$ are all non-negative. According to the property of the eigenvalues of a Kronecker product (see *Theorem 4.2.12* in [31]), we can obtain the eigenvalues of $\bar{\mathbf{L}}$ are all non-negative as well, i.e., $\bar{\mathbf{L}}$ is positive semi-definite.

With Assumption 2, we know that when the number of agents $n \geq 2H+1$, $\bar{\mathbf{G}}$ is full column rank and its pseudoinverse is calculated by $\bar{\mathbf{G}}^+ = (\bar{\mathbf{G}}^\mathsf{T}\bar{\mathbf{G}})^{-1}\bar{\mathbf{G}}^\mathsf{T}$. When the number of agents $n < 2H+1$, $\bar{\mathbf{G}}$ is full row rank and its pseudoinverse is calculated by $\bar{\mathbf{G}}^+ = \bar{\mathbf{G}}^\mathsf{T}(\bar{\mathbf{G}}\bar{\mathbf{G}}^\mathsf{T})^{-1}$ [32].

Based on Assumption 3, we separate the stability analysis into two parts. First, the stability of the controller is analyzed with time-invariant curves (i.e., set-point regulation). Then, the analysis is extended to tracking evolving curves.

Proposition 1: ("many" agents case) Consider a MAS composed of n agents with dynamics (14) and a strongly connected interaction topology $\mathcal{G}$. Given a *time-invariant* curve (4), the controller (20) ensures the asymptotic stability of the position and Fourier coefficients errors $\bar{\mathbf{x}}_e$ and $\boldsymbol{\xi}_e$, when the number of agents is $n \geq 2H+1$ and the control gain k satisfies

$$\begin{cases} 0 < \frac{k_1}{k_2} < -\frac{2}{\Lambda}, & \text{if } \Lambda < 0 \\ k_1, k_2 > 0, & \text{if } \Lambda \geq 0 \end{cases} \tag{21}$$

for $\Lambda = \lambda_{\min}\left(\bar{\mathbf{L}}\bar{\mathbf{G}}\bar{\mathbf{G}}^+ + \bar{\mathbf{G}}\bar{\mathbf{G}}^+\bar{\mathbf{L}}\right)$.

Proof: The proof contains two steps. First, we prove the convergence of $\bar{\mathbf{x}}_e$. By computing the derivative of $\bar{\mathbf{x}}_e$ we obtain the following relations:

$$\begin{aligned}
\dot{\bar{\mathbf{x}}}_e &= \dot{\bar{\mathbf{x}}} \\
&= -k_1\bar{\mathbf{L}}\bar{\mathbf{G}}\boldsymbol{\xi}_e - k_2\bar{\mathbf{x}}_e \\
&= -k_1\bar{\mathbf{L}}\bar{\mathbf{G}}\bar{\mathbf{G}}^+\bar{\mathbf{x}}_e - k_2\bar{\mathbf{x}}_e \\
&= -\mathbf{F}_1\bar{\mathbf{x}}_e
\end{aligned} \tag{22}$$

where $\mathbf{F}_1 = k_1\bar{\mathbf{L}}\bar{\mathbf{G}}\bar{\mathbf{G}}^+ + k_2\mathbf{I}$, which is non-symmetric. Now, let us consider the following symmetric matrix:

$$\mathbf{F}_1 + \mathbf{F}_1^\mathsf{T} = k_1\left(\bar{\mathbf{L}}\bar{\mathbf{G}}\bar{\mathbf{G}}^+ + \bar{\mathbf{G}}\bar{\mathbf{G}}^+\bar{\mathbf{L}}\right) + 2k_2\mathbf{I} \tag{23}$$

It can be seen that both items on the right side of (23) are symmetric matrices. According to the *Theorem 4.3.1* in [33], we know that the eigenvalues of $\mathbf{F}_1 + \mathbf{F}_1^\mathsf{T}$ satisfy the bound:

$$\lambda_{\min}(\mathbf{F}_1 + \mathbf{F}_1^\mathsf{T}) \geq k_1\Lambda + 2k_2. \tag{24}$$

We can see that $\lambda_{\min}(\mathbf{F}_1 + \mathbf{F}_1^\mathsf{T}) > 0$ when k satisfies (21), which implies that all the eigenvalues of $(\mathbf{F}_1 + \mathbf{F}_1^\mathsf{T})/2$ are positive, thus, ensuring that $\mathbf{F}_1$ is positive definite. The solution to the closed-loop dynamic system (22) with initial condition $\bar{\mathbf{x}}_e(0)$ can be computed as follows:

$$\bar{\mathbf{x}}_e(t) = e^{-\mathbf{F}_1 t}\bar{\mathbf{x}}_e(0). \tag{25}$$

which shows that the position error of the agents is asymptotically minimized, i.e., $\bar{\mathbf{x}}_e \to 0$ as $t \to \infty$.

The second part analyzes the convergence of the Fourier coefficients error $\boldsymbol{\xi}_e$, which drives the curve-aligning actions in the controller (20). Note that since $n \geq 2H+1$, the pseudo-inverse of $\bar{\mathbf{G}}$ is computed as $\bar{\mathbf{G}}^+ = (\bar{\mathbf{G}}^\mathsf{T}\bar{\mathbf{G}})^{-1}\bar{\mathbf{G}}^\mathsf{T}$. By using (18) and (17), we obtain the following:

$$\boldsymbol{\xi}_e = \bar{\mathbf{G}}^+\bar{\mathbf{x}}_e + (\bar{\mathbf{G}}^+\bar{\mathbf{G}} - \mathbf{I})\boldsymbol{\xi} = \bar{\mathbf{G}}^+\bar{\mathbf{x}}_e. \tag{26}$$

As $\bar{\mathbf{G}}^+$ has a full row rank, $\bar{\mathbf{x}}_e \to 0$ implies that $\boldsymbol{\xi}_e \to 0$. ∎

Proposition 2: ("few" agents case) Consider a MAS with n agents, dynamics (14) and strongly connected topology $\mathcal{G}$. Given a *time-invariant* curve (4), the controller (20) ensures the asymptotic stability of $\bar{\mathbf{x}}_e$ and the boundedness of $\boldsymbol{\xi}_e$, when $n < 2H+1$.

Proof: As $\bar{\mathbf{G}}^+ = \bar{\mathbf{G}}^\mathsf{T}(\bar{\mathbf{G}}\bar{\mathbf{G}}^\mathsf{T})^{-1}$, the closed-loop system satisfies the following:

$$\begin{aligned}
\dot{\bar{\mathbf{x}}}_e &= \dot{\bar{\mathbf{x}}} \\
&= -k_1\bar{\mathbf{L}}\bar{\mathbf{G}}\boldsymbol{\xi}_e - k_2\bar{\mathbf{x}}_e \\
&= -k_1\bar{\mathbf{L}}\bar{\mathbf{x}}_e - k_2\bar{\mathbf{x}}_e \\
&= -\mathbf{F}_2\bar{\mathbf{x}}_e
\end{aligned} \tag{27}$$

for a positive definite and symmetric matrix $\mathbf{F}_2 = k_1\bar{\mathbf{L}} + k_2\mathbf{I} > 0$. The solution of (27) is

$$\bar{\mathbf{x}}_e(t) = e^{-\mathbf{F}_2 t}\bar{\mathbf{x}}_e(0). \tag{28}$$

which proves the asymptotic stability of $\bar{\mathbf{x}}_e$. To prove the boundedness of the Fourier coefficients error $\boldsymbol{\xi}_e$, we use (17) and (18) to obtain the relation:

$$\boldsymbol{\xi}_e = \bar{\mathbf{G}}^+\bar{\mathbf{x}}_e + (\bar{\mathbf{G}}^+\bar{\mathbf{G}} - \mathbf{I})\boldsymbol{\xi} \tag{29}$$

where by using (28), we can show that

$$\lim_{t\to\infty} \boldsymbol{\xi}_e = (\bar{\mathbf{G}}^+\bar{\mathbf{G}} - \mathbf{I})\boldsymbol{\xi}. \tag{30}$$

This expression implies the boundedness of $\boldsymbol{\xi}_e$, since $\boldsymbol{\xi}$ is constant for time-invariant curves. ∎

Remark 3: Proposition 1 proves that both $\bar{\mathbf{x}}_e$ and $\boldsymbol{\xi}_e$ asymptotically converge to $\mathbf{0}$, which implies that $\bar{\mathbf{u}} \to \mathbf{0}$ as $t \to \infty$ (i.e., zero motion at the equilibrium). Proposition 2 proves asymptotic stability of the linear position error $\bar{\mathbf{x}}_e$ but can only prove boundedness of $\boldsymbol{\xi}_e$. By substituting (30) into (20), we obtain

$$\lim_{t\to\infty} \bar{\mathbf{u}} = -k_1\bar{\mathbf{L}}\underbrace{\bar{\mathbf{G}}(\bar{\mathbf{G}}^+\bar{\mathbf{G}} - \mathbf{I})}_{\mathbf{0}}\boldsymbol{\xi} = \mathbf{0}. \tag{31}$$

Considering $\mathbf{u} = \mathbf{R}^{-1}\bar{\mathbf{u}}$ and since $\mathbf{u}_i = [v_i, \omega_i]^\mathsf{T}$, we can derive the following zero dynamics of orientation:

$$\dot{\theta}_i = 0 \tag{32}$$

which shows that the agents' orientation converges to bounded constant solutions.

Remark 4: Note that static curves have constant Fourier coefficients. However, these coefficients are *time-varying* for evolving curves. Therefore, further analysis should be employed to analyze the stability of our controller in this situation.

Next, we show that the tracking position error vector $\bar{\mathbf{x}}_e$ is bounded on the basis of Propositions 1 and 2. We have shown the processes of approximation of the observed curve by the arc length at a specific time instant in Sec. II-B. The analysis of the tracking errors is based on the Assumption 3.

Before turning to the main analysis, we define several key terms useful for the theory's presentation. Let us denote the sampling period as Δt and the Fourier coefficients of the q-th sampling period as $\boldsymbol{\xi}_q$. We denote the difference of the Fourier coefficients of two neighboring sampling periods as $\Delta\boldsymbol{\xi}_q$, calculated by $\boldsymbol{\xi}_q - \boldsymbol{\xi}_{q+1}$, express a sequence of coefficients differences with the following form:

$$\{\|\bar{\mathbf{G}}\Delta\boldsymbol{\xi}_1\|, \ldots, \|\bar{\mathbf{G}}\Delta\boldsymbol{\xi}_q\|\}. \tag{33}$$

The maximum of (33) is denoted as $\|\bar{\mathbf{G}}\Delta\boldsymbol{\xi}\|_{\max}$. To simplify notation, we introduce the matrix $\bar{\mathbf{F}} \in \{\mathbf{F}_1, \mathbf{F}_2\}$, and denote its minimum eigenvalue as $\varepsilon = \lambda_{\min}(\bar{\mathbf{F}})$.

Proposition 3: (evolving curves) Consider a MAS with n agents, dynamics (14) and strongly connected topology $\mathcal{G}$. Given a *time-varying* curve, the controller (20) ensures the boundedness of the position tracking error $\|\bar{\mathbf{x}}_e\|$ by the positive constant

$$M = \frac{1}{1 - e^{-\varepsilon\Delta t}}\|\bar{\mathbf{G}}\Delta\boldsymbol{\xi}\|_{\max} > 0 \tag{34}$$

if the sampling period and the initial error satisfy the following condition:

$$\Delta t \geq -\frac{1}{\varepsilon}\ln\left(1 - \frac{\|\bar{\mathbf{G}}\Delta\boldsymbol{\xi}\|_{\max}}{\|\bar{\mathbf{x}}_e(0)\|}\right), \tag{35}$$

Proof: The detailed proof is given in Appendix A. ∎

Remark 5: Condition (35) points out that the sampling period can not be too small if we want to ensure the convergence

of tracking errors. It can be derived from (34) that M can reach infinity if we select a very small Δt. Note that the existence of the natural logarithm in (35) requires $\|\bar{\mathbf{x}}_e(0)\| > \|\bar{\mathbf{G}}\Delta\boldsymbol{\xi}\|_{\max}$, which is generally easy to be guaranteed since we have made the slow motion assumption to the curve.

D. Switching Topology

In real-world applications, the communication among agents is usually limited by their relative distance from each other; This means that an agent can only communicate its state with agents within its local neighborhood. Network disruptions, such as unexpected hardware errors and poor signal intensity, can also cause communication failures. In this situation, the multi-agent system is said to interact through a switching topology. The aim of this section is to show that the proposed controller (20) is capable of handling switching topologies.

The presented analysis depends on the extension of Assumptions 1 and 2 in Sec. III-C. When communication failures occur, agents are divided into several subgroups where local communication is preserved. For that, our method relies on the following assumption:

Assumption 4: All the interaction topologies within the subgroups that have more than one agent can be represented by strongly connected and undirected graphs.

We denote the set of all possible graphs as

$$\tilde{\mathcal{G}} = \{\mathcal{G} = (\mathcal{V}, \mathcal{E}, a_{ij})\}. \tag{36}$$

Note that the set $\tilde{\mathcal{G}}$ is finite because the number of agents is also finite.

Proposition 4: Considering Assumption 4, the conclusions from Propositions 1 and 2 still hold for a multi-agent system interacting through switching topologies.

Proof: With a switch topology, the matrix $\bar{\mathbf{L}}$ is not necessarily the Kronecker product of the Laplacian and identity matrices. However, we can always transform $\bar{\mathbf{L}}$ into the following form:

$$\bar{\mathbf{L}}_t = \begin{bmatrix} \mathbf{L}_1 \otimes \mathbf{I} & \cdots & \mathbf{0} & \mathbf{0} \\ \vdots & \ddots & \vdots & \vdots \\ \mathbf{0} & \cdots & \mathbf{L}_\alpha \otimes \mathbf{I} & \mathbf{0} \\ \mathbf{0} & \cdots & \mathbf{0} & \mathbf{I} \end{bmatrix} \tag{37}$$

where $\mathbf{L}_1, \ldots, \mathbf{L}_\alpha$ denote the Laplacians of the interaction graphs of the subgroups, and α is the number of subgroups that contain more than one agent. The identity matrix in $\bar{\mathbf{L}}_t$ (i.e., the last term in the block diagonal) represents the isolated agents that do not interact with other agents.

From the aforementioned assumptions, we know that the matrices $\mathbf{L}_1, \ldots, \mathbf{L}_\alpha$ are symmetric and positive semi-definite, therefore, $\bar{\mathbf{L}}_t$ is symmetric and positive semi-definite. This condition on $\bar{\mathbf{L}}_t$ enables us to directly follow the proofs of Propositions 1 and 2. ∎

Proposition 5: Considering Assumption 3, a multi-agent system with switching topology and driven by the controller (20) can track an evolving curve with bounded position tracking errors.

Proof: According to the proof of Proposition 4, we can find a symmetric and positive semi-definite $\bar{\mathbf{L}}_t$ for a switching topology. Accordingly, we can also obtain a positive definite matrix similar to $\mathbf{F}_1$ or $\mathbf{F}_2$. Denote the matrix as $\mathbf{F}_3$, then we can define the minimum eigenvalues $\varepsilon = \lambda_{\min}(\mathbf{F}_3)$. Follow the procedure of the proof of Proposition 3, then we can prove Proposition 5. ∎

IV. RESULTS

A. Simulation Setup

1) The Observed Curve: We select a curve that evolves in terms of both its shape and the location of its center. We represent the observed curve $\mathbf{c}(s,t)$ by the following time-varying parametric equations:

$$\begin{aligned} c_x(s,t) &= 0.01[4t + (t\sin 4\pi s + 800)\cos 2\pi s] \\ c_y(s,t) &= 0.01[4t + (t\cos 4\pi s + 800)\sin 2\pi s] \end{aligned} \tag{38}$$

The curve starts as a circle and gradually evolves into a parallelogram-like shape.

2) Calculation of the Curve: We sample the points along the curve on a constant parameter step basis. Specifically, we set the constant parameter step as $\delta s = 0.001$, therefore, we collect $N = 1001$ sampled points

The *metric* length of each curve section can be computed by the following curve integral [34]

$$l(s_p, t) = \int_0^{s_p} \sqrt{\left(\frac{\partial c_x(s,t)}{\partial s}\right)^2 + \left(\frac{\partial c_y(s,t)}{\partial s}\right)^2} \, ds \tag{39}$$

where $s_p = (p-1)\delta s$. Note that the analytical computation of (39) usually is difficult. Therefore, in this study, we numerically compute the curve lengths by approximating (39) to:

$$l(s_p, t) \approx \sum_{\kappa=2}^p \|\mathbf{c}(s_\kappa, t) - \mathbf{c}(s_\kappa, t)\|. \tag{40}$$

To approximate the observed curve, we set the number of harmonics to $H = 6$, which provides a compact shape feature vector $\boldsymbol{\xi}$.

3) Formation Control: We perform two types of control tests. In the first, the agents interact with each other through a fixed topology. The interaction topology is established following the rules that the agent i connects to the agent $i-2$, $i-1$, $i+1$, and $i+2$. The weights of all interactions are set to $a_{ij} = 1$. Therefore, the Laplacian of the MAS is:

$$[\mathbf{L}]_{ij} = \begin{cases} -1, & j \in \mathcal{N}_i \\ 4, & j = i \\ 0, & \text{otherwise.} \end{cases} \tag{41}$$

In the second type of test, the agents interact with each other through a switching topology. The interaction topology switches among three modes: (1) all agents interact with their neighbors; (2) some agents interact with each other; (3) none of the agents interact with each other.

The duration of the control test is set to 200 seconds, the sampling period is $\Delta t = 0.1$ seconds, and the feedback gain of the controller is empirically set to $k_1 = 2$ and $k_2 = 1$. We set the distance ℓ as 0.01 m. The agents' positions and orientations at the beginning of each test are set as random values.
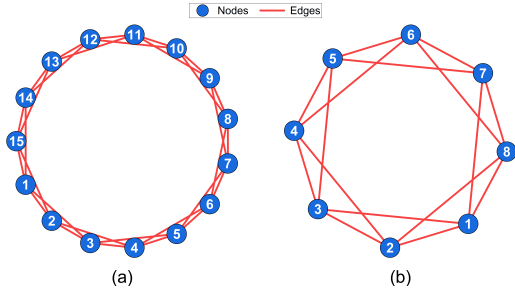
Fig. 4. Fixed topologies: (a) Interaction topology for $n \geq 2H + 1$; (b) Interaction topology for $n < 2H + 1$.
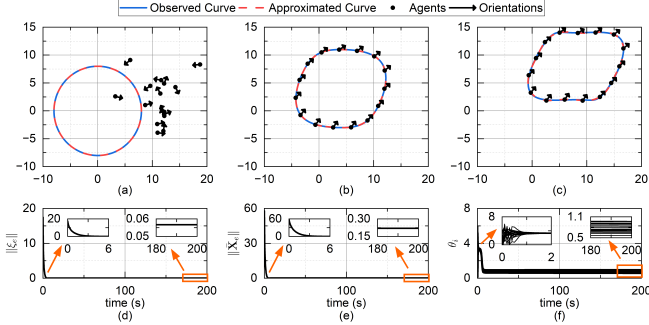

Fig. 5. Simulation results of 15 agents with fixed topology: (a) $t = 0$ s; (b) $t = 100$ s; (c) $t = 200$ s; (d) evolution of $\|\xi_e\|$; (e) evolution of $\|\bar{\mathbf{X}}_e\|$; (f) evolution of agents' orientations.

Fig. 6. Simulation results of 8 agents with fixed topology: (a) $t = 0$ s; (b) $t = 100$ s; (c) $t = 200$ s; (d) evolution of ξ_m; (e) evolution of $\|\bar{\mathbf{X}}_e\|$; (f) evolution of agents' orientations.

In the following sections, we present and analyze some representative simulation results to illustrate the validity of the proposed method. The readers are also referred to the supplementary video (https://vimeo.com/809466573) to check more simulation results.

B. Fixed Topology

1) $n \geq 2H+1$: We set the number of agents to $n = 15$ to ensure $n \geq 2H+1$ in this simulation. The interaction topology of the multi-agent system is shown in Fig. 4(a). It can be calculated that $\Lambda \approx -2.6822 \times 10^{-15}$, therefore, the selected gains satisfy the condition in (21). The minimum sampling period is 3.4364×10^{-4} sec. computed by (35). Therefore, the selected sampling period for the simulation is feasible.

The formation results and the evolution of errors are shown in Fig. 5. As shown in Fig. 5, the approximated curve obtained by (8) fits the observed curve well during the simulation; The agents successfully form the desired curve shape and track the evolving curve under the effects of the proposed formation controller. We record the norm of coefficient errors $\|\xi_e\|$ in Fig. 5(d) and the norm of position errors $\|\mathbf{x}_e\|$ in Fig. 5(e). As is shown, the errors rapidly converge at the beginning stage and remain bounded at the stable stage. We also record the evolution of agents' orientations in Fig. 5(f). It can be seen that the orientations of all agents are bounded when the simulation reaches the stable stage, which meets the conclusion of Remark 3. The results in both figures follow Propositions 1 and 3, which illustrate the validity of the proposed controller.
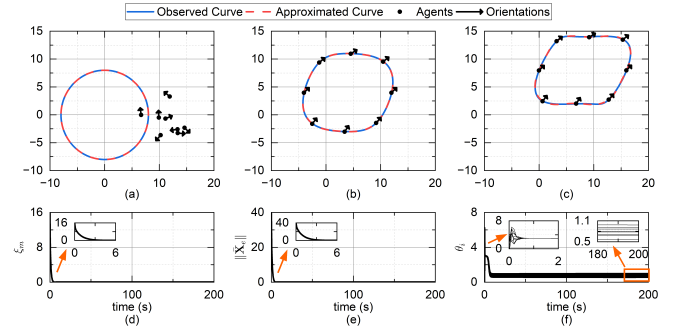
2) $n < 2H+1$: We set the number of agents to $n = 8$ to ensure $n < 2H + 1$ in this simulation. The interaction topology of the multi-agent system is shown in Fig. 4(b). It can be calculated by (35) that the minimum sampling period is 3.4013×10^{-4} sec. Therefore, the selected sampling period for the simulation is feasible.

The formation control results are shown in Fig. 6(a)-(c). We can see that the agents successfully form the desired shape and track the evolving curve under the effects of the proposed controller. The evolution of errors and orientations are shown Fig. 6(d)-(f). As shown in Proposition 2, the coefficient errors ξ_e converge to a limit with the form of (30). For that, we define the following coefficient error metric

$$\xi_m = \left\| \xi_e - (\bar{\mathbf{G}}^+ \bar{\mathbf{G}} - \mathbf{I})\xi \right\| \tag{42}$$

whose evolution during the task can be seen in Fig. 6(d). The metric ξ_m converges to zero as the simulation runs, which agrees with the conclusion of Proposition 2. The norm of position errors shown in Fig. 6(e) converge at the beginning stage and remain bounded as the simulation runs, as proved in Proposition 3. The orientations of agents are shown in Fig. 6(f). We can see that all agents have bounded orientations at the stable stage, which follows the conclusion of Remark 3.

C. Switching Topology

We set the number of agents to $n = 15$. The interaction topologies of the multi-agent system are shown in Fig. 7. As mentioned in Sec. IV-A3, the interaction topology switches among three modes during the simulation. The agents interact with each other through the same topology as the simulation in Sec. IV-B1 until 70 sec, then turn to the topology shown in Fig. 7(b) during 70 sec to 140 sec, and finally turn to the topology shown in Fig. 7(c) after 140 sec. It can be calculated by (35) that the minimum sampling period is 3.4364×10^{-4} sec. Therefore, the selected sampling period for the simulation is feasible.

The formation control results and the evolution of errors are shown in Fig. 8. As shown in Fig. 8, the agents present similar performance compared with the results in Sec. IV-B1. As for the evolution of errors, we can see from Fig. 8(d) and Fig. 8(e) that both the norm of coefficient errors and the absolute norm of errors rapidly converge at the beginning stage and
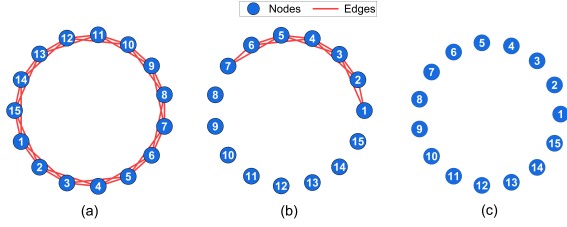
Fig. 7. Switching topologies: (a) the topology for $0\,\mathrm{s} \leq t \leq 70\,\mathrm{s}$; (b) the topology for $70\,\mathrm{s} < t \leq 140\,\mathrm{s}$; (c) the topology for $140\,\mathrm{s} < t \leq 200\,\mathrm{s}$.
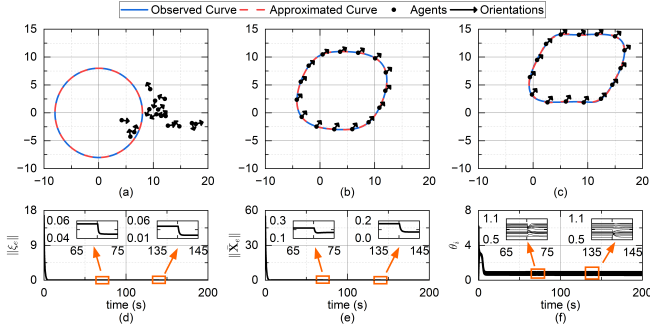
Fig. 8. Simulation results of 15 agents with switching topology: (a) $t = 0\,\mathrm{s}$; (b) $t = 100\,\mathrm{s}$; (c) $t = 200\,\mathrm{s}$; (d) evolution of $\|\xi_e\|$; (e) evolution of $\|\bar{\mathbf{X}}_e\|$; (f) evolution of agents' orientations.

remain bounded at the stable stage despite of sudden changes of topology. The orientations of all agents also follow the conclusion of Remark 3. The results in both figures follow Propositions 4 and 5, which illustrate the validity of the proposed controller in dealing with switching topologies.

D. Experimental Validation

1) Setup: In addition to numerical simulations, we conducted some experiments to verify the performance of the proposed method in a real-world task. These experiments are conducted with the platform shown in Fig. 9, which is composed of nine ($n = 9$) Mona robots [35] with nonholonomic dynamics, a top-view camera to monitor the robots and obtain the feedback pose of the robots, a control PC to collect feedback data and send the motion commands. Wi-Fi communication (at a rate of 10 Hz) between the control PC and robots is built based on ROS. We conduct all experiments in an arena with a size of $1.8\mathrm{m} \times 0.8\mathrm{m}$.

In all experiments, the robots interact through a fixed topology, which is established following the same rule presented in Sec. IV-A3. We empirically set the controller's gains to $k_1 = \frac{2}{3}$ and $k_2 = 2$. Various representative results are presented in the following sections, yet, more experiments can be found in the supplementary video at https://vimeo.com/809466573.

2) $n \geq 2H + 1$: In this experiment, we drive the robots to track an evolving ellipse whose size is growing over time. The equation of the observed curve is:

$$c_x(s,t) = 0.0015[200(1 + 0.01t)\cos 2\pi s + 3t + 400]$$
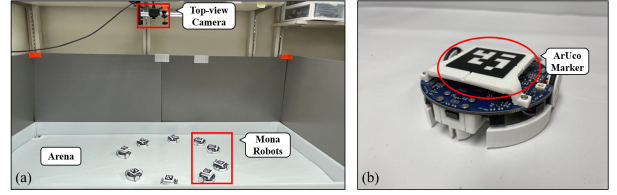$$c_y(s,t) = 0.0015[100(1 + 0.01t)\sin 2\pi s + 300] \tag{43}$$

Fig. 9. The setup of experiments: (a) the configuration of the platform; (b) the Mona robot.

At the beginning of the experiments, all robots have random initial positions and orientations. We set the number of harmonics in the curve approximation to $H = 3$ so that $n \geq 2H + 1$ is ensured. It can be calculated that $\Lambda = -8.8818e \times 10^{-16}$. Therefore, the selected control gains satisfy the condition in (21). As the minimum sampling period is 1.8×10^{-3} seconds (which is computed by (35)), the selected communication frequency is appropriate for the system.

Fig. 10 shows the results of this experiment. Fig. 10(a) depicts various screenshots of the robots during their motion, where we can see how they start from random initial conditions and gradually form the desired evolving shape while keeping track of it. The evolution of the coefficients errors, position errors, and orientations are shown in Fig. 10(b)-(d). From these plots, we can see the asymptotic properties and boundedness of the errors, which follow Proposition 1 and 3. Orientations also reach some bounded values at the stable stage of the experiment, which follows the conclusion of Remark 3.

3) $n < 2H + 1$: In this experiment, we drive the robots to track an evolving curve similar to (38). The curve starts from a circle, then gradually evolves into a parallelogram-like shape. The equation of the observed curve is:

$$c_x(s,t) = 0.0015[(0.5t * \sin 4\pi s + 200)\cos 2\pi s + 3t + 300]$$
$$c_y(s,t) = 0.0015[(0.5t * \cos 4\pi s + 200)\sin 2\pi s + 300] \tag{44}$$

In this case, the number of harmonics is set to $H = 6$ to ensure $n < 2H + 1$. At the beginning of the experiment, all robots have random initial positions and orientations. As the minimum sampling period is 8.2674×10^{-4} seconds (which is computed by (35)), the selected communication frequency is appropriate for the system.

Fig. 11(a) depicts various screenshots of the robots during the experiment. The evolution of the coefficients error, position errors, and orientations are in Fig. 11(b)-(d). These plots similarly show the asymptotic properties and boundedness of the errors. We can also see that all agents have bounded orientations at the stable stage of the experiment, which agrees with the conclusion from Remark 3.

E. Discussion

1) Slow Motion: In the previous analysis, we have made the slow-moving assumption to the curve. In this section, we discuss the influence brought by this assumption. For that, we introduce a speed ratio to evaluate the moving speed of the curve, defined as $r = v_c / v_{\max}$, where v_c denotes the moving speed of the curve and $v_{\max}$ denotes the maximum

Fig. 10. Experiment results of 9 agents with fixed topology: (a) screenshots of experiment result (b) evolution of $\|\xi_e\|$; (c) evolution of $\|\bar{\mathbf{X}}_e\|$; (d) evolution of agents' orientations.
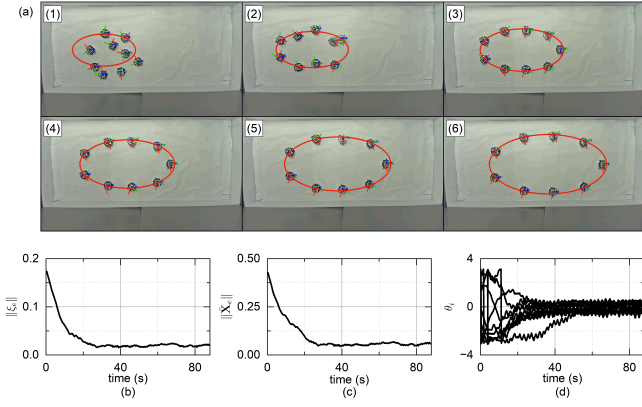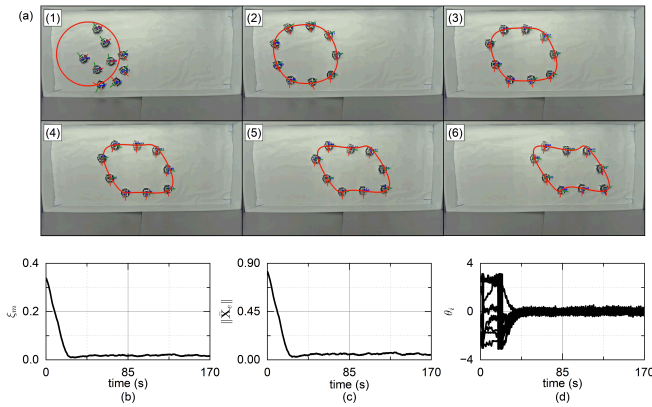

Fig. 11. Experiment results of 9 agents with fixed topology: (a) screenshots of experiment result (b) evolution of $\|\xi_e\|$; (c) evolution of $\|\bar{\mathbf{X}}_e\|$; (d) evolution of agents' orientations.

linear velocity of the agent. It can be derived that $r = 0$ if we don't limit the linear velocity of agents.

Quantitatively measuring the moving speed of a curve is usually difficult. Therefore, instead of adjusting the curve, we set different limitations on the linear velocity of agents to examine the influence of different speed ratios. The results are shown in Table I. The settings of the simulations are the same as Sec. IV-B1 except for the agents' maximum linear velocity and that agents set off from the same straight line with the same initial orientations. We set five different $v_{\max}$ for the agents and record the norm of the position errors $\|\bar{\mathbf{x}}_e\|$ at five different time instances. Table I shows the convergence speed of $\|\bar{\mathbf{x}}_e\|$ decreases as $v_{\max}$ also decreases. When $v_{\max} = 0.1$ m/s, the duration of the simulation is not enough for the MAS to reach the curve. Fig. 12 shows the slow convergence of $\|\bar{\mathbf{x}}_e\|$ with $v_{\max} = 0.1$ m/s.

V. CONCLUSION

In this paper, we study the problem of tracking evolving parametric curves with multiple homogeneous agents. We approximate the observed curve as a Fourier series with arc length parameters, which ensures uniform inter-agent arc length separations. Then, a Fourier-based formation controller

TABLE I
EVOLUTION OF $\|\bar{\mathbf{x}}_e\|$ UNDER DIFFERENT SPEED RATIOS

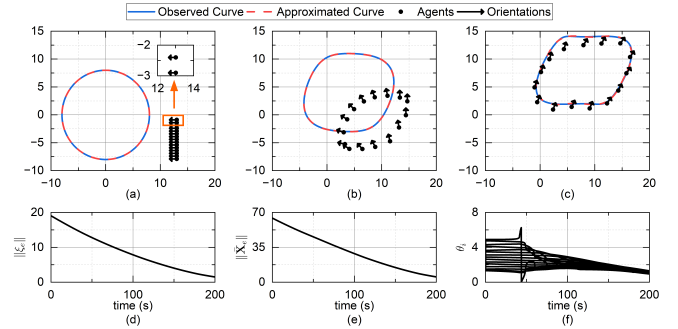| Speed Ratio	30 sec	50 sec	100 sec	150 sec	200 sec
$v_c/0.8$	0.2157	0.2193	0.2193	0.2193	0.2193
$v_c/0.5$	15.3754	0.2193	0.2193	0.2193	0.2193
$v_c/0.3$	33.9787	14.3932	0.2193	0.2193	0.2193
$v_c/0.2$	43.5284	29.7672	1.3307	0.2193	0.2193
$v_c/0.1$	52.5181	45.5192	28.7337	14.7791	5.3363

Fig. 12. Simulation results of 15 agents with $v_{\max} = 0.1$ m/s: (a) $t = 0$ s; (b) $t = 100$ s; (c) $t = 200$ s; (d) evolution of $\|\xi_e\|$; (e) evolution of $\|\bar{\mathbf{X}}_e\|$; (f) evolution of agents' orientations.

is designed to drive the agents to form and track the desired curves. We present a detailed stability analysis of the proposed formation controller and conduct simulations under fixed and switching topologies. Simulation and experiment results show that the proposed controller can drive the agents to form and track the desired curve under both fixed and switching topologies. We also discuss the influence of initial conditions and agents' maximum linear velocity on the performance of the proposed method.

However, the proposed method has various limitations. On the one hand, we have not considered collision avoidance between agents in this paper, which is important in real-world practice. On the other hand, we have only studied agents with nonholonomic dynamics. The formation control of agents with more complex dynamics, such as general non-linear dynamics or dynamics with disturbance [36], needs to be further studied. Future work also includes the formation control with different topology constraints, such as joint connected graphs and directed graphs.

APPENDIX A
PROOF OF PROPOSITION 3

Proof: Let us consider the first sampling period. We denote the position errors of the first sampling period as $\bar{\mathbf{x}}_e^1(t)$ for $t \in [0, \delta t]$. It can be derived that $\bar{\mathbf{x}}_e^1(0) = \bar{\mathbf{x}}_e(0)$. According to (25) and (28), we can obtain

$$\|\bar{\mathbf{x}}_e^1(\Delta t)\| = e^{-\bar{\mathbf{F}}\Delta t}\|\bar{\mathbf{x}}_e(0)\| \leq e^{-\varepsilon\Delta t}\|\bar{\mathbf{x}}_e(0)\|. \qquad (45)$$

Note that $\bar{\mathbf{x}}_e^1(\Delta t)$ is obtained based on the truth that we regard $\boldsymbol{\xi}_1$ as constant during the sampling period. Therefore, there is a difference between $\bar{\mathbf{x}}_e^1(\Delta t)$ and the actual error. Since the end of the first period is the beginning of the second period, we know that the actual Fourier coefficients at the end

of the first period are $\boldsymbol{\xi}_2$. Note that $\bar{\mathbf{x}}_e = \bar{\mathbf{x}} - \bar{\mathbf{G}}\boldsymbol{\xi}$, then we obtain the actual errors at the end of the first period:

$$
\begin{aligned}
\|^a\bar{\mathbf{x}}_e^1\| &= \|\bar{\mathbf{x}} - \bar{\mathbf{G}}\boldsymbol{\xi}_2\| \\
&= \|\bar{\mathbf{x}} - \bar{\mathbf{G}}\boldsymbol{\xi}_1 + \bar{\mathbf{G}}\boldsymbol{\xi}_1 - \bar{\mathbf{G}}\boldsymbol{\xi}_2\| \\
&\leq \|\bar{\mathbf{x}} - \bar{\mathbf{G}}\boldsymbol{\xi}_1\| + \|\bar{\mathbf{G}}(\boldsymbol{\xi}_1 - \boldsymbol{\xi}_2)\| \\
&\leq e^{-\varepsilon\Delta t}\|\bar{\mathbf{x}}_e(0)\| + \|\bar{\mathbf{G}}\Delta\boldsymbol{\xi}_1\|
\end{aligned}
\tag{46}
$$

where $^a\bar{\mathbf{x}}_e^1$ denotes the actual error at the end of the first period.

The actual error at the end of the first period is also the initial error of the second period i.e., $\bar{\mathbf{x}}_e^2(0) =^a \bar{\mathbf{x}}_e^1$. Similarly, we can derive the actual error at the end of the second period:

$$
\begin{aligned}
\|^a\bar{\mathbf{x}}_e^2\| &\leq e^{-\varepsilon\Delta t}\|\bar{\mathbf{x}}_e^2(0)\| + \|\bar{\mathbf{G}}\Delta\boldsymbol{\xi}_2\| \\
&\leq e^{-2\varepsilon\Delta t}\|\bar{\mathbf{x}}_e(0)\| + e^{-\varepsilon\Delta t}\|\bar{\mathbf{G}}\Delta\boldsymbol{\xi}_1\| \\
&\quad + \|\bar{\mathbf{G}}\Delta\boldsymbol{\xi}_2\|.
\end{aligned}
\tag{47}
$$

Accordingly, we can derive the actual error at the end of the q-th period:

$$
\|^a\bar{\mathbf{x}}_e^q\| \leq e^{-q\varepsilon\Delta t}\|\bar{\mathbf{x}}_e(0)\| + \mathrm{E}
\tag{48}
$$

where

$$
\begin{aligned}
\mathbf{E} &= e^{-(q-1)\varepsilon\Delta t}\|\bar{\mathbf{G}}\Delta\boldsymbol{\xi}_1\| \\
&\quad + e^{-(q-2)\varepsilon\Delta t}\|\bar{\mathbf{G}}\Delta\boldsymbol{\xi}_2\| + \cdots + \|\bar{\mathbf{G}}\Delta\boldsymbol{\xi}_q\| \\
&\leq e^{-(q-1)\varepsilon\Delta t}\|\bar{\mathbf{G}}\Delta\boldsymbol{\xi}\|_{\max} + \cdots + \|\bar{\mathbf{G}}\Delta\boldsymbol{\xi}\|_{\max} \\
&= \frac{1 - e^{-q\varepsilon\Delta t}}{1 - e^{-\varepsilon\Delta t}}\|\bar{\mathbf{G}}\Delta\boldsymbol{\xi}\|_{\max}.
\end{aligned}
\tag{49}
$$

We see that, as $q \to \infty$ (i.e., $t \to \infty$),

$$
\lim_{q\to\infty} e^{-q\varepsilon\Delta t}\|\bar{\mathbf{x}}_e(0)\| = 0,
\tag{50}
$$

$$
\mathrm{E} \leq \frac{1}{1 - e^{-\varepsilon\Delta t}}\|\bar{\mathbf{G}}\Delta\boldsymbol{\xi}\|_{\max}.
\tag{51}
$$

Let $M = \frac{1}{1-e^{-\varepsilon\Delta t}}\|\bar{\mathbf{G}}\Delta\boldsymbol{\xi}\|_{\max}$, then we can derive that there always exists a positive constant M such that

$$
\|^a\bar{\mathbf{x}}_e^q\| = \|\bar{\mathbf{x}} - \bar{\mathbf{G}}\boldsymbol{\xi}_{q+1}\| \leq M
\tag{52}
$$

holds as $t \to \infty$, that is, the position errors $\bar{\mathbf{x}}_e$ are always bounded as $t \to \infty$. Considering the condition (35), we can derive that $M \leq \|\bar{\mathbf{x}}_e(0)\|$ always holds, which ensures the decrease of the errors. ∎

REFERENCES

[1] F. Chen and W. Ren, "Multi-agent control: a graph-theoretic perspective," *J. Syst. Sci. Complex.*, vol. 34, no. 5, pp. 1973–2002, Oct. 2021.

[2] R. Olfati-Saber, J. A. Fax, and R. M. Murray, "Consensus and cooperation in networked multi-agent systems," *Proc. IEEE*, vol. 95, no. 1, pp. 215–233, Jan. 2007.

[3] Z. H. Ismail, N. Sariff, and E. Hurtado, "A survey and analysis of cooperative multi-agent robot systems: challenges and directions," in *Applications of Mobile Robots,* London, UK: IntechOpen, 2018, pp. 8–14. [Online]. Available: https://www.intechopen.com/chapters/63854

[4] K. K. Oh, M. C. Park, and H. S. Ahn, "A survey of multi-agent formation control," *Automatica*, vol. 53, pp. 424–440, Mar. 2015.

[5] D. Navarro-Alarcon and Y.-H. Liu, "Fourier-based shape servoing: A new feedback method to actively deform soft objects into desired 2-D image contours," *IEEE Trans. Rob.*, vol. 34, no. 1, pp. 272–279, Feb. 2018.

[6] Z. Zhang, Y. Shi, Z. Zhang, H. Zhang, and S. Bi, "Modified order-reduction method for distributed control of multi-spacecraft networks with time-varying delays," *IEEE Trans. Control Network Syst.*, vol. 5, no. 1, pp. 79–92, Mar. 2018.

[7] Z. Li, Y. Zhao, H. Yan, H. Zhang, L. Zeng, and X. Wang, "Active Disturbance Rejection Formation Tracking Control for Uncertain Nonlinear Multi-Agent Systems With Switching Topology via Dynamic Event-Triggered Extended State Observer," *IEEE Trans. Circuits Syst. I, Reg. Papers*, vol. 70, no. 1, pp. 518-529, Jan. 2023.

[8] H. Zhi, L. Chen, C. Li, and Y. Guo,"Leader–Follower Affine Formation Control of Second-Order Nonlinear Uncertain Multi-Agent Systems," *IEEE Trans. Circuits Syst. II, Exp. Briefs*, vol. 68, no. 12, pp. 3547-3551, Dec. 2021.

[9] X. Liang, H. Wang, Y.-H. Liu, Z. Liu, and W. Chen, "Leader-following formation control of nonholonomic mobile robots with velocity observers," *IEEE/ASME Trans. Mechatron.*, vol. 25, no. 4, pp. 1747–1755, Aug. 2020.

[10] B. Das, B. Subudhi, and B. B. Pati, "Cooperative formation control of autonomous underwater vehicles: an overview," *Int. J. Autom. Comput.*, vol. 13, no. 3, pp. 199–225, Jun. 2016.

[11] S. Susca, F. Bullo, and S. Martinez, "Monitoring environmental boundaries with a robotic sensor network," *IEEE Trans. Control Syst. Technol.*, vol. 16, no. 2, pp. 288–296, Mar. 2008.

[12] D. W. Casbeer, D. B. Kingston, R. W. Beard, and T. W. McLain, "Cooperative forest fire surveillance using a team of small unmanned air vehicles," *Int. J. Syst. Sci.*, vol. 37, no. 6, pp. 351–360, May 2006.

[13] W. Ren and E. Atkins, "Distributed multi-vehicle coordinated control via local information exchange," *Int. J. Robust Nonlinear Control*, vol. 17, no. 10-11, pp. 1002–1033, Jul. 2007.

[14] D. Zhang, Y. Tang, W. Zhang, and X. Wu, "Hierarchical design for position-based formation control of rotorcraft-like aerial vehicles," *IEEE Trans. Control Network Syst.*, vol. 7, no. 4, pp. 1789–1800, Dec. 2020.

[15] X. Wang, B. Zerr, H. Thomas, B. Clement, and Z. Xie, "Pattern formation of multi-auv systems with the optical sensor based on displacement-based formation control," *Int. J. Syst. Sci.*, vol. 51, no. 2, pp. 348–367, Jan. 2020.

[16] H. G. de Marina, "Maneuvering and robustness issues in undirected displacement-consensus-based formation control," *IEEE Trans. Autom. Control*, vol. 66, no. 7, pp. 3370–3377, Jul. 2021.

[17] E. D. Ferreira-Vazquez, E. G. Hernández-Martínez, J.-J. Flores-Godoy, G. Fernandez-Anaya, and P. Paniagua-Contro, "Distance-based formation control using angular information between robots," *J. Intell. Robot. Syst.*, vol. 83, no. 3, pp. 543–560, Sep. 2016.

[18] Y. B. Bae, Y. H. Lim, and H. S. Ahn, "Distributed robust adaptive gradient controller in distance-based formation control with exogenous disturbance," *IEEE Trans. Autom. Control*, vol. 66, no. 6, pp. 2868–2874, Jun. 2020.

[19] J. Shao, L. Shi, Y. Cheng, and T. Li, "Asynchronous Tracking Control of Leader–Follower Multiagent Systems With Input Uncertainties Over Switching Signed Digraphs," *IEEE Trans. Cybern.*, vol. 52, no. 7, pp. 6379–6390, Jul. 2022.

[20] S. Kalantar and U. R. Zimmer, "A formation control approach to adaptation of contour-shaped robotic formations," in *Proc. 2006 IEEE/RSJ Int. Conf. Intell. Robots Syst.,* Beijing, China, Oct. 2006, pp. 1490–1497.

[21] A. L. Bertozzi, M. Kemp, and D. Marthaler, "Determining environmental boundaries: asynchronous communication and physical scales," in *Cooperative Control*, V. Kumar, N. Leonard, A. S. Morse, Eds. Berlin, Germany: Springer, 2005, pp. 25–42. [Online]. Available: https://doi.org/10.1007/978-3-540-31595-7_2

[22] S. Li, Y. Guo, and B. Bingham, "Multi-robot cooperative control for monitoring and tracking dynamic plumes," in *Proc. 2014 IEEE Int. Conf. Robot. Autom.,* Hong Kong, China, Sep. 2014, pp. 67–73.

[23] D. Saldaña, R. Assunção, M. A. Hsieh, M. F. Campos, and V. Kumar, "Estimating boundary dynamics using robotic sensor networks with pointwise measurements," *Auton. Robots*, vol. 45, no. 2, pp. 193–208, Feb. 2021.

[24] J. W. Wang, Y. Guo, M. Fahad, and B. Bingham, "Dynamic Plume Tracking by Cooperative Robots," *IEEE/ASME Trans. Mechatron.*, vol. 24, no. 2, pp. 609–620, Apr. 2019.

[25] L. Feng and J. Katupitiya, "Vector Field based Control of Quadrotor UAVs for Wildfire Boundary Monitoring," *J. Intell. Robot. Syst.*, vol. 106, no. 1, pp. 1–27, Sep. 2022.

[26] J. Qi, G. Ma, J. Zhu, P. Zhou, Y. Lyu, H. Zhang, and D. Navarro-Alarcon, "Contour moments based manipulation of composite rigid-deformable objects with finite time model estimation and shape/position control," *IEEE/ASME Trans. Mechatron.*, early access, Dec. 03, 2021, DOI: 10.1109/TMECH.2021.3126383.

[27] P. Zhou, J. Zhu, S. Huo, and D. Navarro-Alarcon, "Lasesom: A latent and semantic representation framework for soft object manipulation," *IEEE Rob. Autom. Lett.*, vol. 6, no. 3, pp. 5381–5388, Jul. 2021.

[28] M. Mesbahi and M. Egerstedt, "Graph theory," in *Graph Theoretic Methods in Multiagent Networks,* Princeton, NJ, USA: Princeton University Press, 2010, pp. 14–41.

[29] P. Lu, Z. Wu, S. Baldi and W. Yu, "Distributed Disturbance-and-Leader Estimation for Controlling Networks of Nonholonomic Mobile Robots," *IEEE Trans. Circuits Syst. I Reg. Papers*, vol. 69, no. 9, pp. 3762-3771, Sept. 2022.

[30] H. M. Becerra, J. A. Colunga, and J. G. Romero, "Simultaneous convergence of position and orientation of wheeled mobile robots using trajectory planning and robust controllers," *Int. J. Adv. Rob. Syst.*, vol. 15, no. 1 pp. 1–18, Jan. 2018.

[31] R. A. Horn and C. R. Johnson, "Matrix equations and the Kronecker product," in *Topics in Matrix Analysis,* 1st ed. New York, NY, USA: Cambridge University Press, 1991, pp. 245.

[32] J. C. A. Barata and M. S. Hussein, "The moore–penrose pseudoinverse: A tutorial review of the theory," *Braz. J. Phys.*, vol. 42, no. 1, pp. 146–165, Apr. 2012.

[33] R. A. Horn and C. R. Johnson, "Hermitian matrices, symmetric matrices, and congruences," in *Matrix Analysis,* 2nd ed. New York, NY, USA: Cambridge University Press, 2012, pp. 225-312.

[34] J. Stewart, "Parametric equations and polar coordinates," in *Multivariable Calculus,* 7th ed. Belmont, CA, USA: Cengage Learning, 2010, pp. 659–712.

[35] F. Arvin, J. Espinosa, B. Bird, A. West, S. Watson, and B. Lennox, "Mona: An affordable open-source mobile robot for education and research," *J. Intell. Rob. Syst.*, vol. 94, pp.761–775, Jun. 2019.

[36] J. G. Romero, D. Navarro-Alarcon, E. Nuño, and H. Que, "A globally convergent adaptive velocity observer for nonholonomic mobile robots affected by unknown disturbances," *IEEE Control Syst. Lett.*, vol. 7, pp. 85–90, 2023. Accessed on Jun. 27, 2022, DOI:10.1109/LCSYS.2022.3186621.

Jose Guadalupe Romero (Member, IEEE) obtained the Ph.D. degree in Control Theory from the University of Paris-Sud XI, France in 2013. Currently, he is a full time Professor at ITAM in Mexico and since 2019 he has been the Director of undergraduate mechatronics engineering program. He has over 45 papers in peer-reviewed international journals where he has also served as a reviewer. His research interests are focused on nonlinear and adaptive control, stability analysis and the state estimation problem, with application to mechanical systems, aerial vehicles, mobile robots and multi-agent systems. He currently serves as an Editor of the INTERNATIONAL JOURNAL OF ADAPTIVE CONTROL AND SIGNAL PROCESSING.

Luiza Labazanova received her MS degree in Space and Engineering Systems from Skolkovo Institute of Science and Technology, Moscow, in 2019. She was a visiting research student in Kaji-lab at the University of Electro-Communications, Tokyo, working in the field of haptics. Currently, she is working toward a Ph.D. degree in mechanical engineering at The Hong Kong Polytechnic University. Her research interests include hybrid robotics, artificial intelligence, and multi-agent systems.

Anqing Duan received his Ph.D. degree in robotics from the Italian Institute of Technology and the University of Genoa in 2021. Since 2021, he has been a Research Associate with the Robotics and Machine Intelligence Laboratory at The Hong Kong Polytechnic University. His research interest lies in multi-agent systems.

Bin Zhang received his bachelor's degree in detection, guidance and control technology from Beihang University, Beijing, China, in 2017, and his master's degree in control science and engineering from China Academy of Space Technology, Beijing, China, in 2020. Since 2021, he has been pursuing a Ph.D. degree in mechanical engineering at The Hong Kong Polytechnic University, Kowloon, Hong Kong. His current research interests include multi-agent systems and control theory.

Xiang Li (Senior Member, IEEE) received the Ph.D. degree from Nanyang Technological University, Singapore, in 2013. Since 2019, he has been an Associate Professor at Tsinghua University, China. His current research interests include robotic manipulation, vision-based control, micro/nano robots, and human–robot interaction. He was an Associate Editor of the IEEE ROBOTICS AND AUTOMATION MAGAZINE from 2019 to 2021, and currently serves as Associate Editor of IEEE ROBOTICS AND AUTOMATION LETTERS.

Hui Zhi received her bachelor's degree in control science and engineering from Beijing University of Chemical Technology, Beijing, China, and her master's degree in control science and engineering from Harbin Institute of Technology, Harbin, China. Since 2022, she has been pursuing a Ph.D. degree in mechanical engineering at The Hong Kong Polytechnic University, Kowloon, Hong Kong. Her current research interests include multi-agent formation control and control theory.

David Navarro-Alarcon (Senior Member, IEEE) received the Ph.D. degree in mechanical and automation engineering from The Chinese University of Hong Kong, in 2014. Since 2017, he has been with The Hong Kong Polytechnic University, where he is currently an Associate Professor with the Department of Mechanical Engineering, and the Principal Investigator of the Robotics and Machine Intelligence Laboratory. His current research interests include perceptual robotics and control systems. He currently serves as an Associate Editor of the IEEE TRANSACTIONS ON ROBOTICS.